Anisotropic chloride transport in 3D printed concrete and its dependence on layer height and interface types

Sahil Surehali[1], Avinaya Tripathi[1], Atharwa Samir Nimbalkar[1], Narayanan Neithalath[2]

Abstract

Layered concrete systems, such as those obtained using 3D printing, demonstrates inter-layer and inter-filament defects, which influence transport of moisture and ionic species through the structural element, thus impacting its durability. The printing parameters, including the layer height and width, and printing rate, dictates the number and quality of the interfaces, rendering a directional dependence to the transport of moisture and deleterious ions. This work focuses on the impact of layer heights (6, 13, and 20 mm) and transport directions (along the direction of printing, along the direction of layer build-up, and in the direction perpendicular to the above two directions), on the non-steady state chloride migration coefficients (D_{nssm}) of 3D printed concretes. The direction-dependent D_{nssm} values of the printed samples are 10-30% higher than those of companion cast samples. Interrogation of the microstructure of the printed samples through porosity and electrical conductivity, along with the transport quantification, establishes the influence of anisotropy on the transport properties. The inter-filament interfaces are shown to be more detrimental from an ionic transport standpoint, thereby providing guidelines on choosing the printing direction with respect to the direction of ionic ingress.

Keywords: 3D printing; ionic transport; non-steady state migration; porosity; anisotropy

---

[1] Graduate student, School of Sustainable Engineering and Built Environment, Arizona State University, Tempe AZ 85287

[2] Professor, School of Sustainable Engineering and Built Environment, Arizona State University, Tempe AZ 85287; Corresponding author: e-mail: Narayanan.Neithalath@asu.edu

1. Introduction

Additive manufacturing (AM) or 3D printing is an emerging technology for building 3D structures from a digital model. 3D concrete printing has gained significant attention in the recent past, primarily because of its ability to eliminate formwork for concrete construction, thereby enabling the construction of complex and sophisticated, structurally- and functionally-efficient geometries. 3D printing results in the reduction of the overall construction cost by 35-60% [1], [2]. Moreover, it can eliminate 30-60% of construction wastes, thereby enhancing the sustainability of concrete construction, and at the same time, diminishing labor costs and production time by 50-70% [3], [4]. Other potential advantages include: (a) enhanced safety by eliminating dangerous activities (such as working at heights on scaffolding); (b) allowing material deposition at high precision, minimizing the chances of errors; (c) increasing architectural freedom; (d) enabling the potential of multifunctionality of structural/architectural elements; and (e) creation of high-end technology-based jobs in construction [5]–[7].

Extrusion-based printing technique is currently the most widely explored method for in-situ and pre-cast concrete 3D printing applications. This technique extrudes material from a digitally controlled nozzle mounted on a gantry or robotic arm to print a structure layer-by-layer [8]–[10]. A number of studies have examined the materials- and process-related aspects that influence the rheological characteristics such as pumpability, extrudability, and buildability, that are critical towards successful concrete 3D printing [8], [11]–[15]. The mechanical properties of 3D printed concrete elements have also been studied in detail [16]–[22]. However, the durability aspects of 3D printed concrete have received relatively less attention, even though the unique aspects related to 3D printing, including layering and anisotropy have the potential to significantly impact the durability. Layer-by-layer extrusion method of 3D printing has the potential to result in increased void fraction, especially at the interface of the layers and filaments [23], [24]. Moreover, the lack of compaction also results in the bulk of the material being more porous as compared to conventionally cast concretes. Although it has been shown that more porous (than the bulk) interfaces induce anisotropy on the mechanical properties of 3D printed concrete [7], [12], [17], [19], [25]–[27], print geometry alterations and adjustments in the printing parameters are capable of mitigating those effects to a great extent. It has been reported that the inter-layer zone acts similar to cracks, and offers minimal resistance to the transport of deleterious species, potentially reducing the durability of 3D concrete printed elements [28]–[31]. The lack of non-uniform pore water evaporation is reported to result in a non-uniform shrinkage at the interlayer zones and, thus, significant reduction in interlayer bond strength and enhancement in moisture permeability and higher chloride penetration [32]. The rate of interfacial strength loss in 3D concrete printed elements under the action of repeated freeze/thaw cycles is reported to be 2 to 3-times higher than the rate of compressive and flexural strength loss, revealing the vulnerability of interfaces to frost attack [30]. The interconnected or continuous voids at the interlayer zones, orientation of aggregates/fibers, and pore size and distribution have been postulated to lead to a directional dependence of durability parameters in 3D printed concrete structures [33]–[35]. The variation in print parameters (layer height, filament width, rate of printing etc.) results in differences in the bulk microstructure within a layer, as well as in the interface type (inter-layer and inter-filament), the orientation of the interfaces, and the length of transport through these interfaces, when tested along different directions. This necessitates in-depth investigations on ionic transport in extrusion-printed concrete elements, which is the focus of this paper. Directional dependence of mechanical properties have been elucidated elsewhere [21], [36]–[39].

Among the several process parameters involved in 3D concrete printing, this study explores the influence of layer dimensions and the directional dependence on the chloride transport resistance of plain and basalt fiber-reinforced 3D printed mortars. In order to ensure consistency, other parameters such as the print speed, nozzle shape and diameter, nozzle offset distance, etc., are kept constant, even though some of them also have the potential to impact the properties. The 3D printed specimens are moist-cured for 28 days before testing to ensure that drying does not cause any undesirable interface defects. Non-steady state migration (NSSM) test is employed to evaluate the chloride ion ingress into the mixtures, since the lower voltages eliminate joule heating effects that are commonly encountered in rapid chloride permeability test (RCPT) of concrete. Moreover, acceleration of ionic transport under high voltages (such as 60 V commonly used in RCPT) in more porous specimens, or through less resistive transport paths in otherwise dense specimens, results in breakthrough transport within a few minutes and current overflow, resulting in abrupt stoppage of the test, lending tests such as RCPT generally unsuitable for 3D printed specimens. Here, NSSM tests are carried out on specimens extracted by coring 3D printed prisms along three orthogonal directions – along the direction of printing, along the direction of layer build-up, and in the direction perpendicular to the above two directions - to explore the directional dependence of chloride ion penetration resistance, in addition to the effect of layer heights.

2. Experimental Program

2.1. Materials and mixtures

The materials used in the study include Type I/II Ordinary Portland Cement (OPC) conforming to ASTM C 150, limestone (L) powder conforming to ASTM C 568 [40], and commercial sand (M) with a median particle size of 0.20 mm, conforming to ASTMC C 778 [41]. The chemical and physical properties of the constituents are tabulated in Table 1. Chopped basalt fibers (BF), 15 mm long and 0.04-0.06 mm in diameter, were used as fiber reinforcement. The characteristics and mechanical properties of the basalt fibers are shown in Table 2. The mixture proportions were derived from the authors' past work [15], [21], [42] and are shown in Table 3. Since the intent of the paper is to investigate the influence of layer heights and the transport direction with respect to the printing process, the investigation is limited to the two mixtures shown in Table 3. All the mixtures contain 50% sand by mass of the total solids in the mortar. A polycarboxylate ether-based superplasticizer (0.25%-0.35% by mass of binder) was used in all the mixtures. While many 3D printed concrete mixtures use steel fibers to enhance mechanical properties, such mixtures are not used in this study since the presence of conductive steel fibers make accelerated chloride transport tests untenable.

Table 1: Composition and properties of the mortar constituents

Constituent	Chemical composition (% by mass)							d_{50} (μm)	Specific gravity
	SiO_2	Al_2O_3	Fe_2O_3	CaO	MgO	SO_3	LOI*		
OPC	19.60	4.09	3.39	63.21	3.37	3.17	2.54	10.4	3.15
Limestone(L)	$CaCO_3$>99%							1.5	2.70
Medium Sand (M)	SiO_2>99%							200	2.40
*Loss on Ignition									

Table 2: Properties of the chopped basalt fibers

Fiber type	Diameter (mm)	Length (mm)	Specific gravity	Tensile Strength (GPa)	Young's Modulus (GPa)
Chopped Basalt Fiber (BF)	0.04 - 0.06	15	2.36	0.28	18

Table 3: Mixture proportions

Mixture ID	Mass Fraction of Ingredients			Chopped Basalt Fiber (BF)$^+$	Water-to-binder ratio (w/b) by mass	SP to binder ratio (SP%) by mass of the binder
	OPC	Limestone (L)	Sand (M)			
L_{30}	0.35	0.15	0.5	-	0.35	0.25
$L_{30\text{ - BF}}$	0.35	0.15	0.5	0.28	0.35	0.35
$^+$Percentage by volume of the mixture						

2.2. 3D printing of mortars

The selected mixtures (Table 3) were printed using a gantry-based 3D printer equipped with a screw extrusion system, as shown in Figure 1. A circular nozzle, 20 mm in diameter, was used to print filaments of a specified layer height (LH) and a fixed layer width (LW) of 20 mm. It has been reported that the specimens printed using layer heights larger than the nozzle diameter results in larger voids because of the absence of a vertical pressing force and improper filament overlap in the plane of printing [21]. Thus, layer heights smaller than or equal to the nozzle diameter are preferred, so as to induce some transverse flow to ensure filament overlap under the vertical nozzle pressure while extruding the layers, and thus to minimize the potential print defects. The print layer heights selected for the study were 6, 13, and 20 mm. Slabs were printed at a constant in-plane print speed of 50 mm/s, and the stepper for the screw extruder was calibrated for a flow rate of approximately 6, 13, and 20 mL/s for layer heights of 6, 13, and 20 mm respectively. Figure 2 shows the idealized 3D models of printed elements of size 200 × 200 × 200 mm, having different layer heights. The 3D printed mortar mixtures were moist-cured in a chamber at 23±2°C and >98% relative humidity (RH) for 28 days, after which the test specimens of desired sizes were cut from the printed elements.

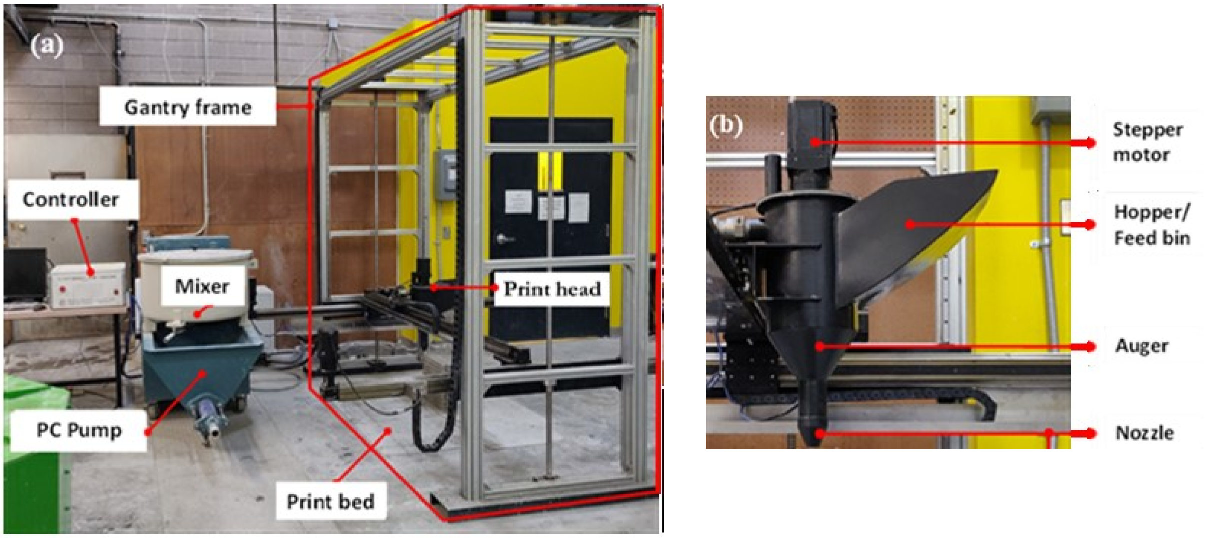

Figure 1: Printer setup showing: (a) the gantry printer with the controller and the mixer, and (b) close up of the print head.

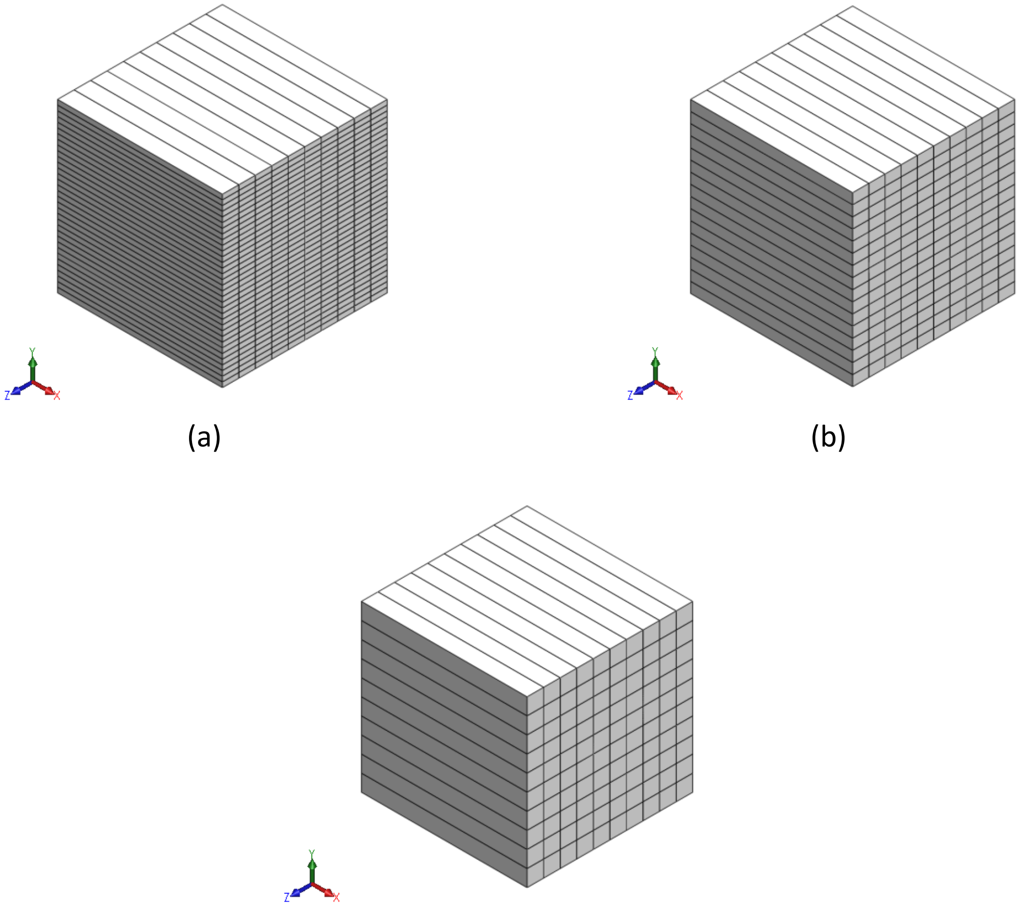

(a)

(b)

(c)

Figure 2: Representative 3D models of cubes (200 × 200 × 200 mm) extracted from slabs printed using layer-heights of: (a) 6 mm, (b) 13 mm, and (c) 20 mm. Note that the layer widths are the same for all cases.

2.3. Test specimen preparation

In this study, direction-1 (D1) is defined as along the direction of printing, direction-2 (D2) represents the direction of layer-build-up, and the direction perpendicular to both D1 and D2 is denoted as direction-3 (D3). In Figure 3(a), D1, D2, and D3 correspond to the X, Y, and Z axes, respectively. Cylinders of 100 mm diameter and 200 mm length were cored from the printed slabs in all the three directions, as shown in Figures 3(b)-(d), and the transport tests carried out on 50 mm thick discs sliced from the cored cylinders. The specimens were tested in three mutually orthogonal directions since the migrating species will encounter different types and number of interfaces in each direction due to the layered system, potentially resulting in an anisotropic behavior. The ionic transport in the accelerated chloride transport tests is parallel to (i.e., along) both the inter-layer and inter-filament interfaces in the D1 direction, while it is perpendicular to the inter-layer and inter-filament interfaces in D2 and D3 directions, respectively. The number of inter-layer and inter-filament interfaces in the 50 mm thick discs are different for different layer heights. Figure 4 shows in detail the predominant transport paths in all three test directions for specimens with the three different layer heights used in the study. Note that, as is typical in accelerated migration tests, 1D transport is assumed. In addition, Table 4 summarizes the type and length of interfaces (inter-layer or inter-filament) on the surface of specimen exposed to chloride ions since it depends on the direction of test and the print layer height, respectively.

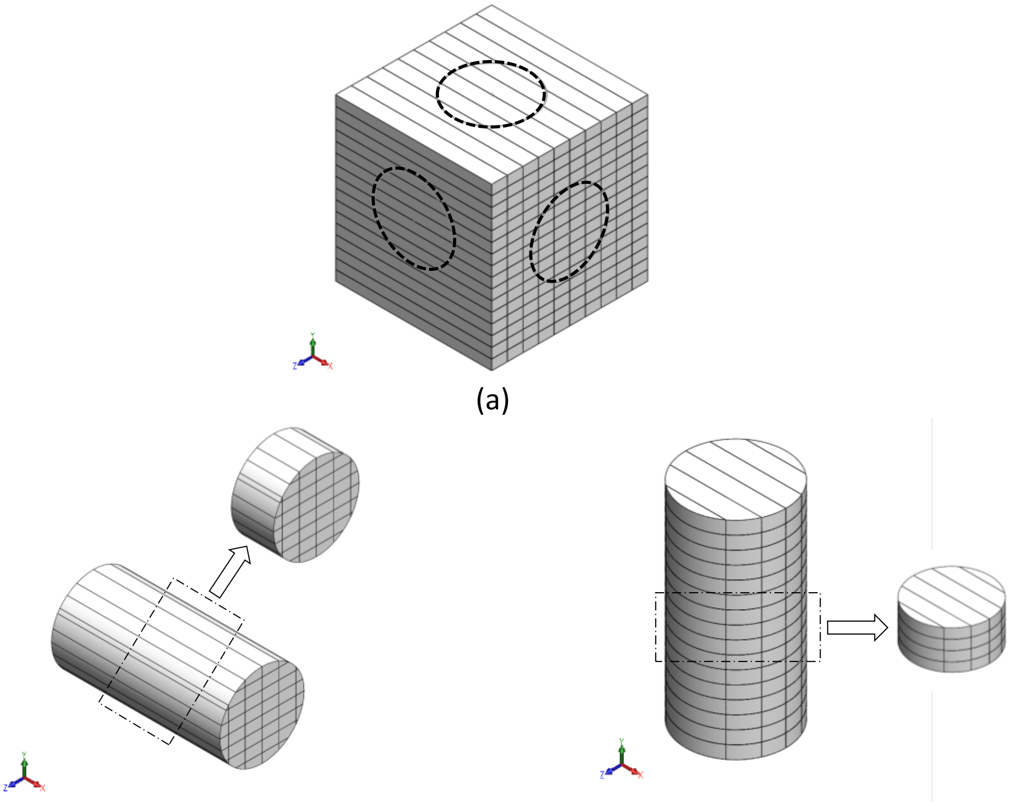

(a)

(b)

(c)

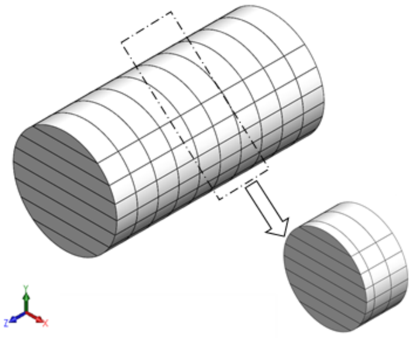

(d)

Figure 3: Test specimen preparation details: (a) representation of three coring directions in the 3D printed slabs. Sliced 50 mm thick discs from 200 mm × 100 mm cylinders cored in directions: (b) D1, (c) D2, and (d) D3.

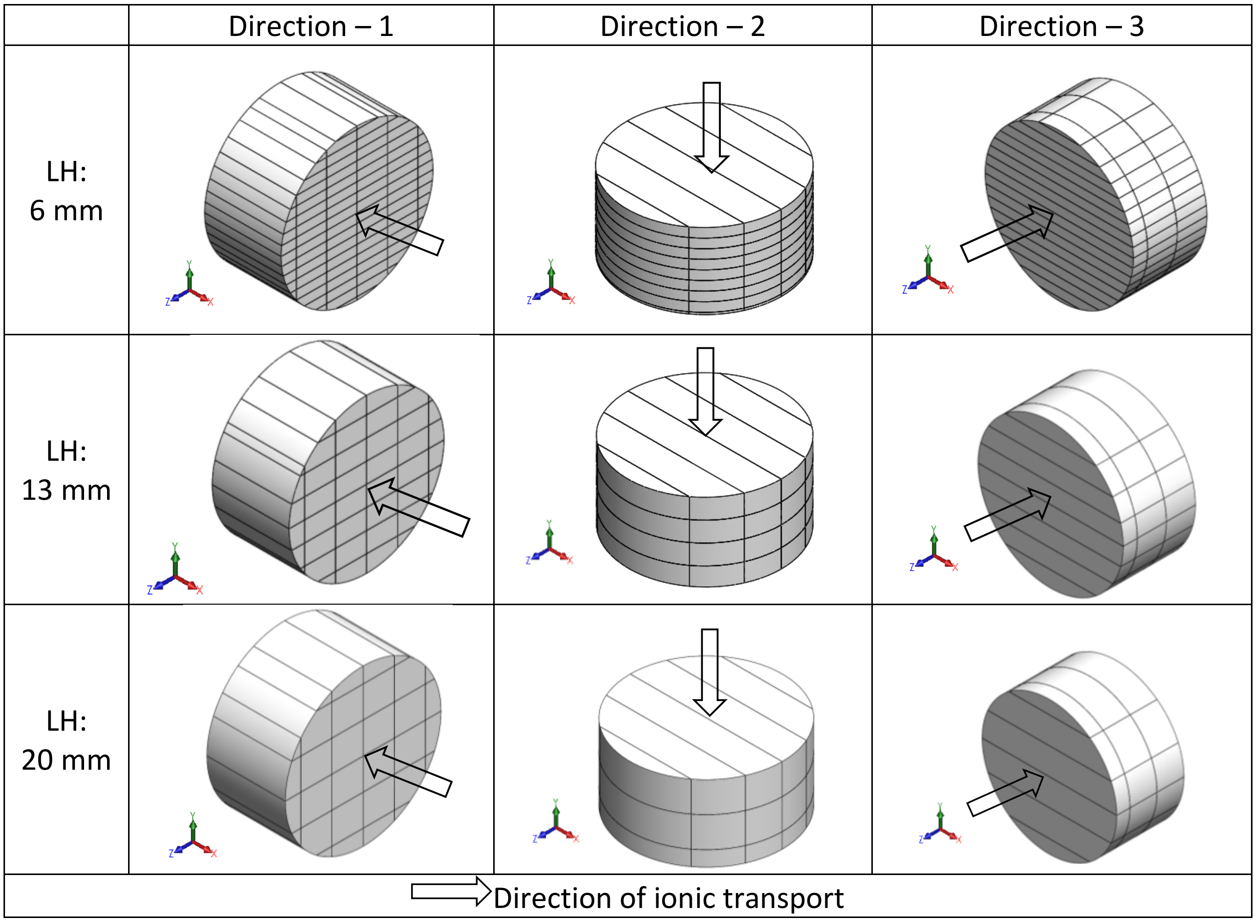

Figure 4: Schematic representation of ionic transport paths in different directions for specimens printed using different layer heights. The lighter shade corresponds to the filaments, and the darker shade, to the layers.

Table 4: Type and length of interfaces on the surface exposed to ionic transport

	Direction – 1	Direction – 2	Direction – 3
Type of interface	Interlayer and interfilament	Interfilament	Interlayer
Total length of interface (mm) in a 100 mm diameter × 50 mm thick disc			
LH: 6 mm	1719.10	403.30	1317.98
LH: 13 mm	1020.21	403.30	583.40
LH: 20 mm	806.60	403.30	403.30

2.4. Test Methods

2.4.1. Non-steady state migration (NSSM) test

NSSM tests were performed for each test direction and layer height under consideration in accordance with NT BUILD 492 [43]. The samples were vacuum saturated for 3 h; saturated lime solution was then added to the vacuum chamber while maintaining the vacuum; and vacuum saturation continued for an additional hour. The specimens were then left undisturbed in the solution for 20 h. The specimens were then enclosed between a catholyte cell, filled with 2 N NaCl solution, and an anolyte cell, filled with 0.3 N NaOH solution. Initially, a 30 V potential was applied, and the initial current passing through the specimen was noted. The initial current for all specimens varied from 120 to 180 mA, primarily due to the less dense interfaces in 3D printed concrete specimens, as has been mentioned elsewhere [23], [28], [39]. Therefore, based on the voltage adjustment suggested in NT BUILD 492 [43], all specimens were subjected to a 10 V potential for 24 h. After the test duration, the specimens were axially split, and 0.1 N silver nitrate ($AgNO_3$) solution was sprayed on the freshly split sections. The chloride penetration depth was then measured from the white silver chloride precipitation. A digital Vernier caliper was used to measure the depths along several points on the cut specimens. A digital image analysis procedure (using ImageJ© software) was also used to independently confirm the measurements. The NSSM values, D_{nssm}, were calculated using the penetration depth as:

$$D_{nssm} = \frac{RT}{zFE}\frac{x_d - \alpha\sqrt{x_d}}{t} \tag{1}$$

where R is the molar gas constant (8.314 J/K.mol), z is the absolute value of ion valence (1 for chloride ions), F is the Faraday constant (9.648×10^4 J/(V.mol)), T is the average value of the initial and final temperatures in the anolyte solution in K, x_d is the average value of penetration depths in m, and t is the test duration in seconds.

The terms E and α in Eq. (1) are given by:

$$E = \frac{U-2}{L} \tag{2a}$$

$$\alpha = 2\sqrt{\frac{\mathrm{RT}}{\mathrm{zFE}}} \times \mathrm{erf}^{-1}\left(1 - \frac{2\,\mathrm{C_d}}{\mathrm{C_0}}\right) \quad (2b)$$

where *U* is the absolute value of the applied voltage in volts, *L* is the thickness of the specimen in m, C_d is the chloride concentration at which white silver chloride precipitate ($C_d \approx 0.07$ N), and C_0 is the chloride concentration in the catholyte solution (2 N).

2.4.2. Determination of porosity using vacuum saturation

The capillary porosities of 28-day cured mortar specimens were determined using the vacuum saturation method elaborated in RILEM CPC 11.3 [44]. 50 mm thick discs were cut from 100 mm × 200 mm cylinders and oven-dried to a constant mass to remove all the evaporable water. The masses of the oven-dried specimens were measured after allowing them to return to room temperature. The specimens were subjected to vacuum saturation for 3 h; water was then added into the vacuum chamber while the vacuum was maintained; and the vacuuming continued for an additional 1 h. The specimens were then left undisturbed in water for 20 more hours. The masses of the specimens were then recorded. The difference in the masses, converted into volume, represents the volume of capillary pores. The capillary porosity was calculated by dividing the volume of capillary pores by the volume of the concrete specimen. Average values of porosities determined from two or more companion specimens were used for the analysis.

2.4.3. Mercury intrusion porosimetry

MIP is commonly used to evaluate the pore structure of cementitious materials [45], [46]. The representative sections from 28-days cured samples, sliced carefully from the *bulk region* of the filaments using a diamond-tipped saw, were subjected to MIP to determine the effect of different layer heights on the porosity of printed material. It was ensured that the inter-filament and interlayer interfaces were not included in the test specimen, so as to obtain the properties of the bulk portion of the layer corresponding to different layer heights. A mercury intrusion porosimeter that can generate a maximum pressure of 414 MPa and evaluate a minimum pore diameter of 0.001 μm was used. The test was performed in two stages - the low-pressure step evacuates the pores, fills them with mercury, and carries out pressurization to 414 kPa, while the high-pressure step imposes pressures up to 414 MPa. The applied pressure during the intrusion of mercury and pore diameter are related through the Washburn equation as:

$$\Delta \mathrm{P} = \frac{-2\,\sigma \cos\theta}{\mathrm{r}} \quad (3)$$

where $\Delta \mathrm{P}$ is the pressure required for mercury intrusion, *r* is radius of the pore being intruded, σ is the surface tension of mercury, and θ is the contact angle between the mercury and pore wall. The contact angle and surface tension of mercury used were 130^{o} and 0.485 N/m, respectively [46]. Data was also recorded during the pressurization and depressurization steps.

2.4.4. Electrical properties

The bulk electrical resistivity of specimens was determined in accordance with ASTM C1876 [47]. All the specimens were submerged in a simulated pore solution (lime-saturated; conductivity of 7.87 S/m) for at least 6 days before carrying out the resistivity measurements. The resistivity measurements were taken at 1 KHz frequency using a commercial concrete resistivity meter (RCON2^{TM}). To maintain good contact between the electrodes and samples, a sponge soaked in lime saturated solution was used as a conductive medium between the samples and electrodes. The bulk resistances (R_b) of the specimens were also determined using electrical impedance spectroscopy (EIS) using a Solartron^{TM} 1260 gain-phase analyzer operating in a frequency range of 1 Hz to 10 MHz. A 250 mV AC signal was employed, and 10 measurements per decade of frequency were recorded.

The different test methods used in this work and the sample characteristics are summarized in Table 5.

Table 5. Test methods and experimental matrix

Experiments	Test standard	Parameters studied	Specimen geometry	Specimens tested
Non-steady state migration test	NT BUILD 492 [43]	• Specimen preparation method (Cast and 3D printed) • Mixtures (L_{30} and $L_{30\text{ - }BF}$) • Layer height (6, 13, and 20 mm) • Directions (D1, D2, and D3)	Cylindrical discs (100 × 50 mm)	40
Vacuum saturation	RILEM CPC 11.3 [44]		Cylindrical discs (100 × 50 mm)	40
Mercury intrusion porosimetry*	[45], [46]		Small pieces taken from layer bulk	16
Bulk electrical resistivity	ASTM C1876 [47]		Cylindrical discs (100 × 50 mm)	40
* Directional dependence is not considered in MIP tests since only the bulk is characterized				

3. Results and Discussions

3.1. Porosity and pore structure

The capillary porosities of the 3D printed specimens determined using vacuum saturation are shown in Figures 5(a) and (b). The porosities of cast samples were determined to be 22.9±0.2%, and they are observed not to differ substantially with the addition of basalt fibers. The capillary porosities of all the printed specimens are slightly higher (up to ~5%) than those of the cast specimens, in accordance with established literature. The porosity variation with print direction and layer heights for the printed samples are shown in Figure 5. The higher porosities of the printed samples can be partly attributed to the elimination of vibration during the 3D printing process. Figure 5(a) shows the capillary porosities of the printed samples as a function of direction, obtained by averaging the porosities recorded for a specific direction for all three layer heights used. It can be observed that the capillary porosities are generally invariant with the direction of printing. Since the overall porosities of cylindrical specimens (of dimensions used for the NSSM test) are determined in this case, and there are layers and interfaces in all directions, the values are rather similar. Similarly, the influence of layer height is also found to be minimal as can be noticed from Figure 5(b), when overall porosities are measured. However, the differences are more evident from MIP results shown below. Also, notice that the capillary porosity measurements described in this work cannot determine pore sizes larger than 0.5 mm (since water will not be retained in such voids, because they are likely to be connected). Larger layer heights introduce larger interfilament voids [21], as will also be shown later in this paper. Thus, the transport (and electrical property) dependence on porosity is not strictly captured by capillary porosity measurements, and results in only slight differences based on layer heights or printing directions, as shown here.

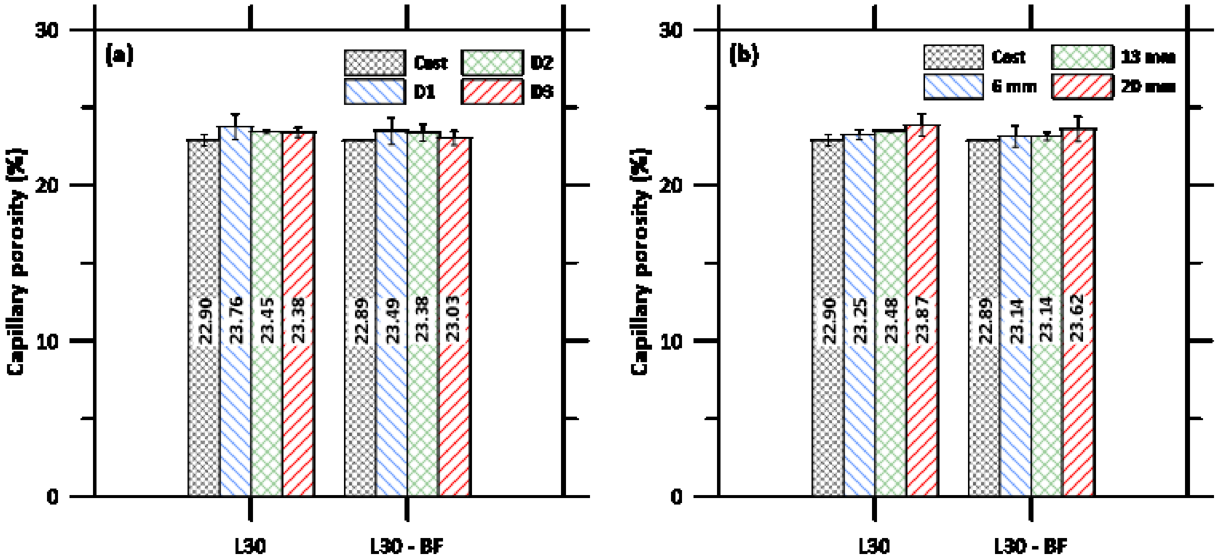

Figure 5: Capillary porosity of the printed samples: (a) along the three directions of testing, and (b) with varying layer heights.

Figures 6 and 7 demonstrate the cumulative pore volumes and pore size distributions in the samples printed using different layer heights. Note that the samples were extracted from the bulk portion of the layers, and thus the values shown here do not represent the effects of interfaces. However, the nozzle pressure variations with difference in layer heights (notwithstanding the adjustment in flow rate – see Section 2.2), are primarily responsible for the differences in porosity and pore structure features with different layer heights. Table 6 lists the pertinent information from MIP for all the samples. The cumulative pore volumes are higher in the printed mortars as compared to the cast mortars, as shown in Figure 6, which is an effect of consolidation/vibration when the specimens are cast. A small increase in the cumulative volume intruded is noticed with increasing layer heights, which is a result of the slightly higher pressures applied by the print head to achieve smaller layer heights [21]. Compared to the cast samples, the cumulative volumes intruded detected by MIP was found to increase by approximately 9, 21, and 33% for the samples with layer heights of 6, 13, and 20 mm, respectively, in the case of unreinforced mixture, and by approximately 3, 12, and 28% in the case of fiber-reinforced mixture.

In porous media, the intrusion and subsequent extrusion of mercury results in a hysteresis, where the extrusion curve lies above the intrusion curve (see Figure 6), indicating that mercury is retained in the sample after the sample has been de-pressurized [48], [49]. The volume of mercury retained has been primarily attributed to the pore structure of the sample; in particular pores with small diameter openings which open to larger pores, often referred to as the ink-bottle pores [50]. While the difference in the contact angle between mercury and the pore wall in the intrusion cycle versus the extrusion cycle could also be a factor [52], this aspect has not been considered in this paper. The retained volume is reported to be related to the tortuosity of the pore structure, since a more tortuous pore structure renders evacuation of mercury more difficult after the pressure is removed. A retention factor (R), which is the ratio of the retained volume to the total intruded volume, gives a better idea of the complexity of the pore structure – a larger retention factor indicating a more tortuous pore structure. It has also been shown that the retention factor decreases with an increase in critical pore diameter [53],and the same is true with porosity as well. Table 6 shows that the cast specimens demonstrate the highest retention factor, due largely to the consolidation/vibration of such mixtures that result in a tortuous pore structure. For printed specimens, the retention factor decreases with an increase in layer height, indicating decreased tortuosity of the pore system. The retention factor of the printed samples with a 6 mm thick layer is somewhat close to that of the cast sample, although this applies to only the bulk portion of the layer. If the interfaces are also considered (which is not in the scope of this work), it is expected that the retention factor will be higher for the samples with 6 mm thick layer as opposed to 20 mm thick layer, because the higher nozzle pressure for a smaller layer height will likely result in a less porous interface. Figure 7 shows that the peak pore diameter is also higher for the printed samples (especially for non-fiber reinforced mixtures). The addition of basalt fibers results in increase in the critical pore size of the cast specimens, as has been reported [54], [55]. The pore size distribution curves are not found to be significantly different with layer heights in the printed samples, even though there is a small increase in the critical pore size with increasing layer height.

As mentioned earlier, the porosities obtained from the vacuum saturation method and MIP are not directly comparable, since the capillary porosities were measured on the specimen including inter-layer and inter-filament interfaces, while the MIP tests were carried out on samples extracted from within the bulk of the filament. In addition, both the method evaluates pore sizes in different ranges, which explains the difference in the total porosities obtained from these methods. However, assuming that the difference between the vacuum saturation porosity and MIP porosity can be attributed to the large pores beyond the ~100 μm range that MIP measures, it can be noticed that approximately 12-14% of the porosity is from larger voids in the sample, which are likely the inter-filament and inter-layer porosities. This will be shown later in the paper.

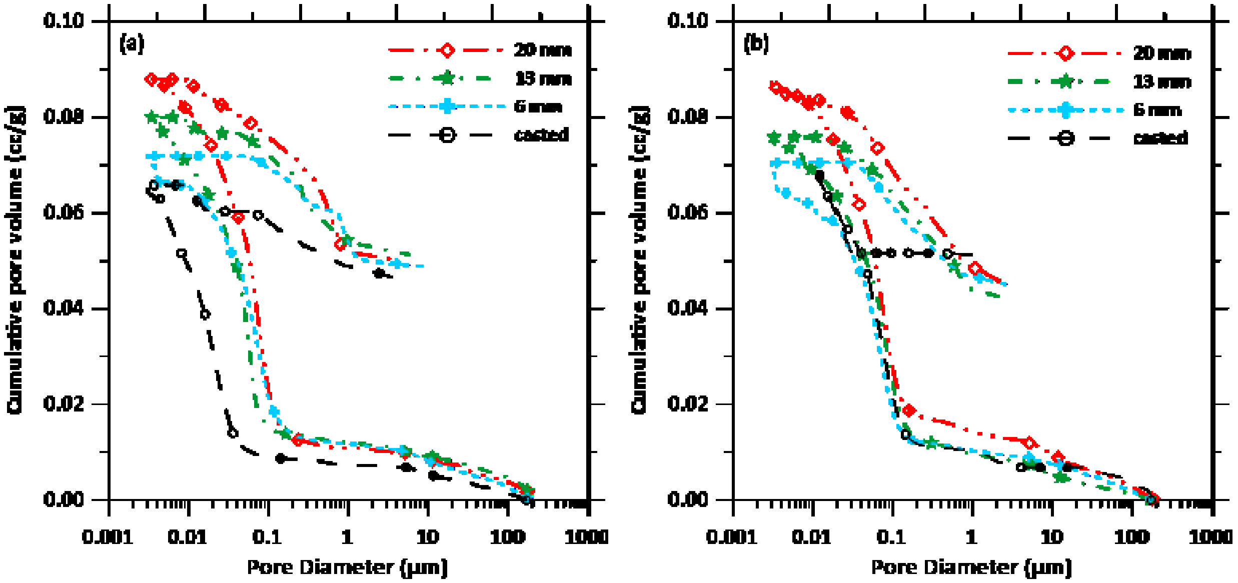

Figure 6: Representsative cumulative pore volume curves for: (a) L_{30} mixture, and (b) L_{30-BF} mixture. Both the intrusion (bottom) and extrusion (top) curves are shown

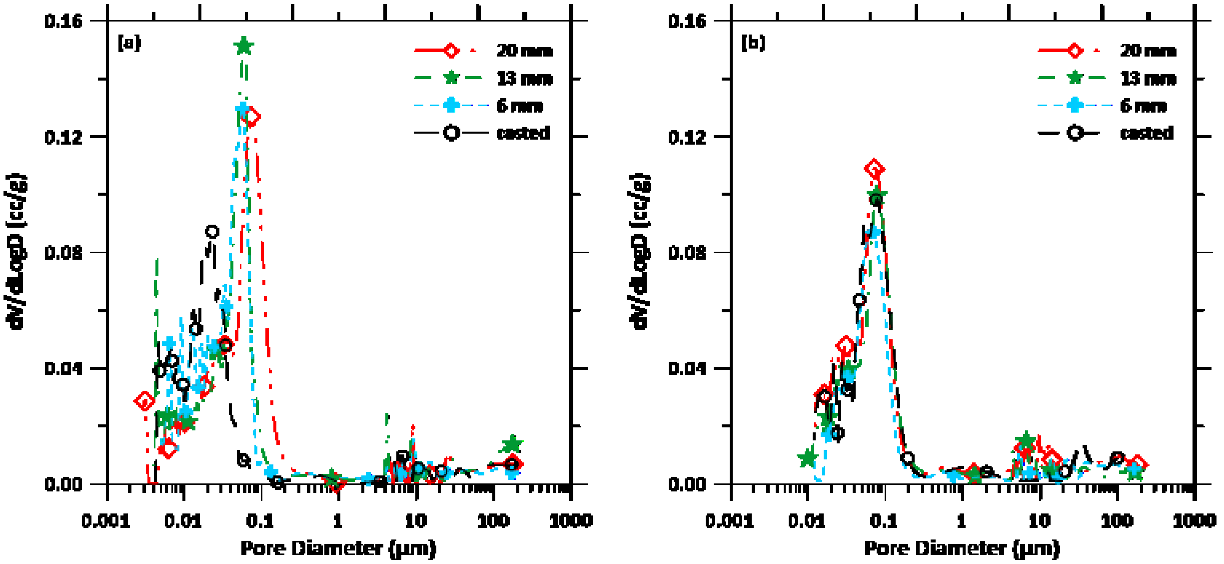

Figure 7: Pore size distribution curves for: (a) L_{30} mixture, and (b) L_{30-BF} mixture.

Table 6: Pore structure information from MIP.

Mixture	Specimen preparation method	Layer height (mm)	Cum. vol. intruded (cc/g)	Vol. of mercury retained (cc/g)	Porosity (%)	Critical pore diameter (nm)	Retention factor, R (%)
L_{30}	Cast	-*	0.066	0.039	14.48	22.91	59.09
	Printed	6	0.072	0.039	15.82	57.72	54.17
		13	0.080	0.041	17.60	60.35	51.25
		20	0.088	0.040	19.34	74.91	45.45
$L_{30\text{-}BF}$	Cast	-*	0.068	0.042	14.96	78.46	61.76
	Printed	6	0.070	0.036	15.47	66.26	51.43
		13	0.076	0.033	16.72	78.57	43.42
		20	0.087	0.032	19.23	76.45	36.78
	* Layer height parameter not applicable for casted specimens						

3.2. Bulk electrical properties

The bulk electrical resistivity of all the specimens were determined using DC resistivity and AC-EIS spectra, and both provided very similar outputs as shown in Figure 8. The remainder of the analysis uses the conductivities obtained from DC resistivity testing. The conductivities of the specimens are shown in Figures 9(a) and (b) – the former for plain and basalt fiber reinforced mixtures for different layer heights, averaged across all three directions, and the latter, as a function of directions based on samples extracted to carry out the chloride ion transport tests. Such averaging helps to demonstrate the response succinctly as a function of both layer heights and directions. Even though the conductivity is also a bulk property, it is influenced by the total pore volume and the connectivity of the conduction paths. Figure 9(a) shows that the conductivity of both the plain and fiber reinforced mixtures increases with layer height, which is in line with the higher porosity in the bulk regions of higher layer height mixtures, as shown in Figure 6. This is an argument favoring the construction of 3D printed structures using lower layer heights, which have also been shown to result in better mechanical properties [21]. The basalt fiber reinforced mixtures demonstrate slightly lower conductivities than their unreinforced counterparts, which also has been reported in some studies as an effect of its pore filling nature (e.g., reduced connectivities, even when pore volumes are slightly higher [56]–[59]). Figure 9(b) shows the conductivity of the printed specimens as a function of the directions of chloride migration testing. Here, we do not consider the explicit effect of layer height, and the conductivities of specimens with all three layer heights in a particular direction are averaged in order to highlight the effect of anisotropy in electrical transport, which is similar to that in chloride transport, which will be shown in the following section. Note that the conductivities measured along directions D2 and D3 are very similar, whereas the conductivity along direction D1 is marginally higher.

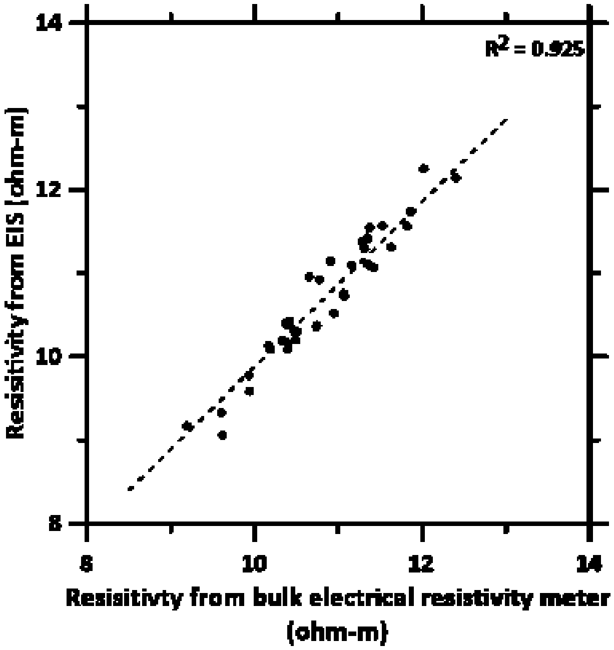

Figure 8: Correlation between electrical resistivities obtained from DC electrical resistivity test and AC electrical impedance spectroscopy.

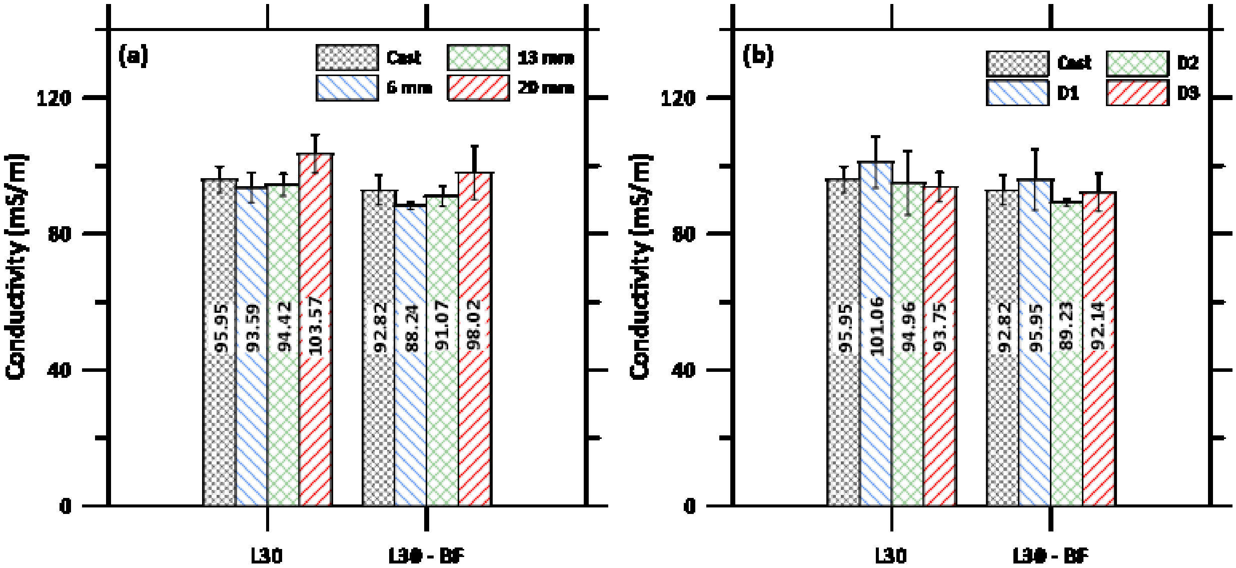

Figure 9: Bulk electrical conductivity of the printed specimens obtained from resistivity meter as a function of: (a) layer heights, and (b) directions based on samples extracted to carry out the chloride ion transport tests.

To examine this behavior further, Figure 10 shows the cross sections of cylinders cut perpendicular to the D1 direction, for specimens with print layer heights of 6, 13, and 20 mm. It is immediately observed that, as the layer heights increase, larger inter-filament voids are present in the specimen. These voids are in the direction of measurement of conductivity, rendering a higher pore connectivity to the sample in this direction, and consequently increasing the conductivity values. More experimental observations of this effect and discussions are provided in the section on chloride transport.


(a) (b) (c)

Figure 10: Representative cross-sections showing voids formed at the inter-filament interfaces for layer heights of: (a) 6 mm, (b) 13 mm, and (c) 20 mm. The figures show cross-sections along direction D1, which is into the plane of the images.

3.3. Non-steady state migration (NSSM) coefficients

NSSM tests were carried out for the plain and fiber-reinforced slabs printed using three different layer heights, and specimens extracted in the three different orthogonal directions as shown in Figure 3. Figures 11(a) and (b) show the non-steady-state migration coefficients (D_{nssm}) for all the samples. The cast samples showed a D_{nssm} value of 15.0±2.4 $\times 10^{-12}$ m^2/s, and 18.3±2.5 $\times 10^{-12}$ m^2/s for L_{30} and L_{30-BF} mixtures, respectively, which is in line with the D_{nssm} values reported for concretes containing high volume of filler materials such as limestone, even under a 30 V potential [60]–[62]. Note that all the samples here were tested for 24 h using a voltage of 10 V, the reason for which was explained earlier. An analysis of voltage dependence of D_{nssm} is shown later in this section. As would be expected, the 3D printed specimens show 20-30% higher D_{nssm} values as compared to the cast specimen, depending on the layer heights and the orientation of testing. The differences in migration coefficients between 3D printed plain and basalt fiber reinforced mixtures are rather minimal.

In Figure 11, for the direction D1, two different sets of D_{nssm} values are reported (denoted as $D1_A$ and $D1_B$), which requires some context. Direction D1 has both inter-filament and inter-layer interfaces running along the direction of transport, making it a dominant transport direction. This can be easily comprehended from the data in Table 4, where the total length of the inter-filament and inter-layer interfaces on the transport plane is much higher in the direction D1 as compared to directions D2 and D3, which have either inter-filament or inter-layer interfaces in the transport plane. As mentioned in the previous section, the average conductivity measured along the direction D1 was higher than those in directions D2 and D3, which were similar. Figure 10 also shows that, for larger layer heights, the inter-filament voids traverse the entire cross section along direction D1. Figures 12 and 13 shows the cut cross-sections of the sample after the chloride migration test. As an example, for the 6 mm layer height specimen, it can be noticed from Figure 12 that, in the direction D1, chloride ions have penetrated 21.8 mm from the surface along the inter-filament interface, as opposed to 14.1 mm in the bulk (as noted from the white silver chloride precipitate). The migration coefficients calculated based on the penetration depth in the bulk (as is typical for cast specimens – e.g., using a depth of 14.1 mm for the specimen with 6 mm layer height) is denoted as $D1_A$ in Figure 11.

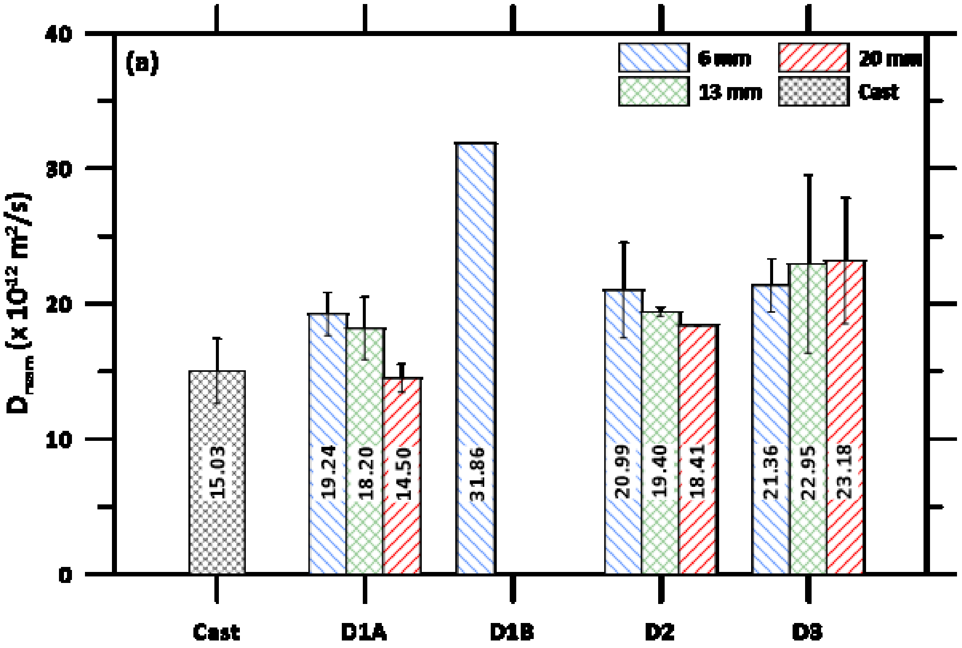

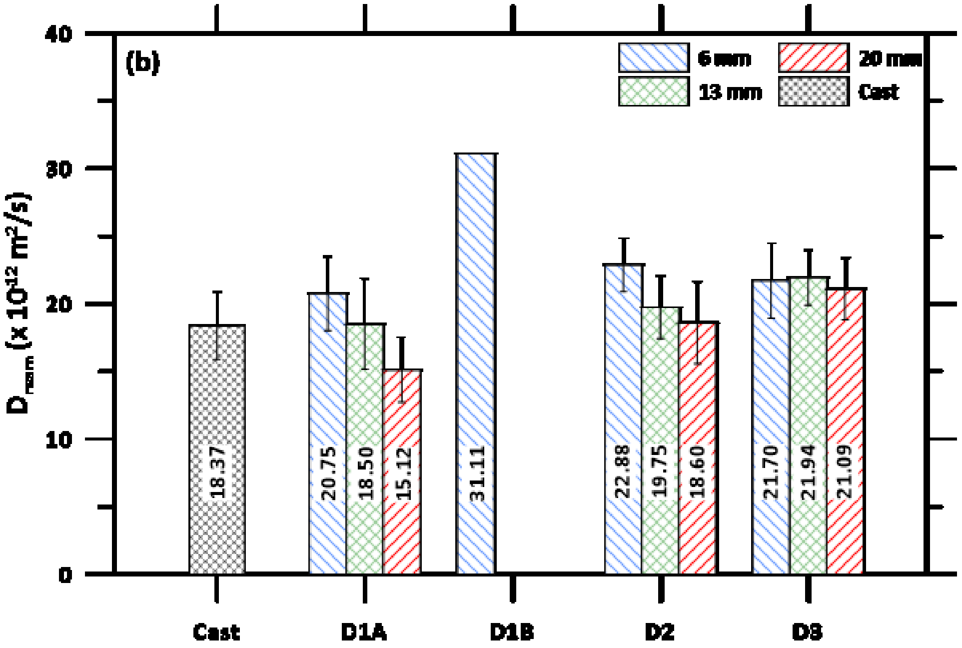

Figure 11: Non-steady state migration coefficients for the 3D printed samples: (a) L_{30} mixture, and (b) L_{30-BF} mixture. D_{1B} is not indicated for the 13 mm and 20 mm layer height samples because the chlorides penetrated the entire depth of the specimen.

The enhanced penetration along the inter-filament interface results in a migration coefficient enhancement of about 1.5 times in the direction D1 (denoted as D_{1B} in Figure 11), which is denoted as $D1_B$. For the 13 mm and 20 mm layer height specimens, in the direction D1, Figures 12 and 13 show that the chloride ions have penetrated the sample completely along the inter-filament interfaces, even before the end of the test duration (still under 10 V), causing current overflow and early termination of the test. Thus, the D_{nssm} values could not be accurately calculated for these samples, and thus $D1_B$ values cannot be reported for these samples. The D_{nssm} values denoted as $D1_A$ for the 13 and 20 mm samples are calculated based on a penetration depth of 13.4±1.35 mm, and 11.9±0.67 mm respectively for the L_{30} mixture, even though the ions have penetrated the entire depth through the inter-filament interfaces. Thus, in general, it is desirable to ignore the calculated migration coefficients in the D1 direction (along the direction of printing), irrespective of the layer height, since the multiple transport pathways (through the bulk and the interfaces) provide unreliable estimates of the actual transport. For directions D2 and D3, this is generally not an issue for all layer heights as can be noticed from Figures 12 and 13 (for plain and basalt fiber reinforced concretes).

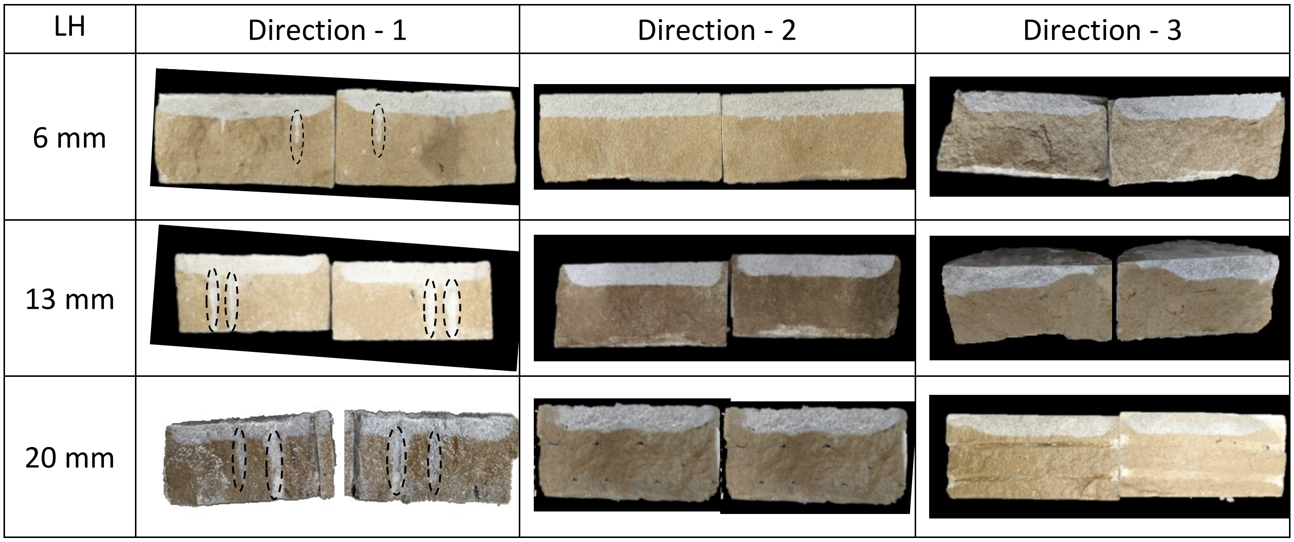

Figure 12: Axially split samples, along the three directions, of 3D printed L_{30} mortar samples after the NSSM test and spraying silver nitrate. The oval highlights the chloride ingress path in the samples tested in –direction D1 for all layer heights.

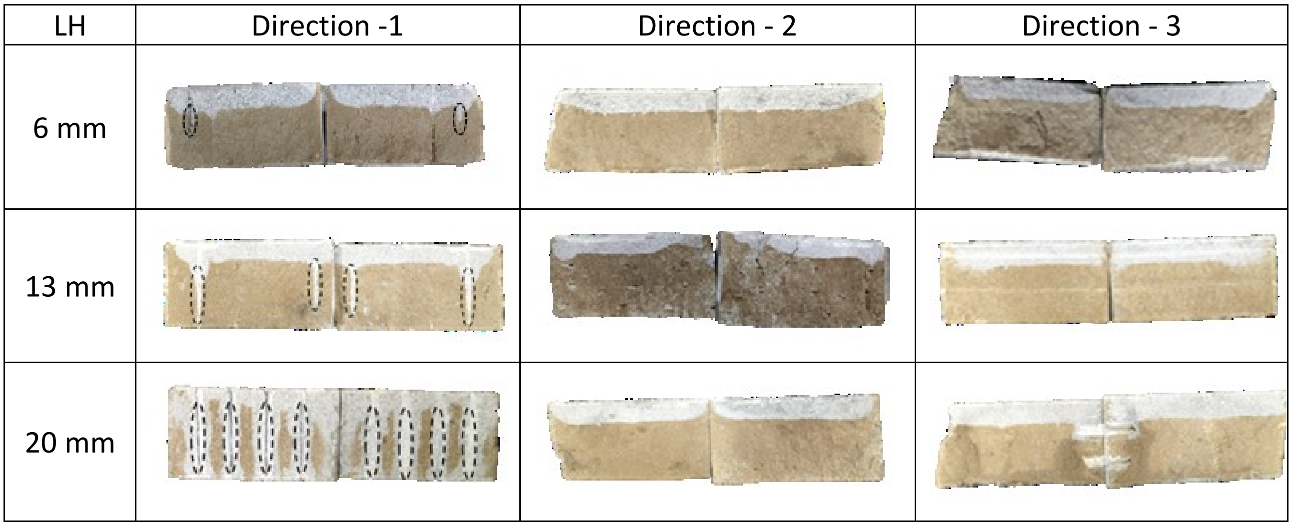

Figure 13: Axially split samples, along the three directions, of 3D printed $L_{30\text{-BF}}$ mortar samples after the NSSM test and spraying silver nitrate. The oval highlights the chloride ingress path in the samples tested in –direction D1 for all layer heights.

The D_{nssm} values in the D2 and D3 directions are rather close to each other for different layer heights, as seen from Figure 11, in line with the conductivity values. In the D2 direction, the higher D_{nssm} values observed in the 6 mm layer height specimens can be attributed to the larger number of inter-layer interfaces intersecting the direction of transport. The plane of transport has the same number of inter-filament interfaces in this case, irrespective of layer heights (see Figure 4) because of the constant layer widths used in printing, and thus the differences in D_{nssm} for different layer heights for both plain and fiber reinforced specimens can simply be attributed to the number of inter-layer interfaces that the ions have to penetrate (notwithstanding the reduced porosity and pore sizes in the bulk for the 6 mm layer height specimen). In Direction D3, there are a greater number of inter-layer interfaces in the plane of transport for the 6 mm layer height specimen, than for the 20 mm layer height specimen, but the number of inter-filament interfaces are the same irrespective of the layer height (see Figure 4). Since the interfaces perpendicular to (or intersecting) the direction of transport is more critical, and since there are equal number of such interfaces in the D3 direction, it is not surprising that the D_{nssm} values are rather invariant with the layer heights.

The foregoing discussion points to the fact that, for 3D printed samples, the inter-layer and inter-filament interfaces are bigger determinants of the ionic transport process under electrical acceleration. It is desirable to choose print parameters and print direction in such a manner as to minimize the number of interfaces in the plane and in the direction of ionic transport. Inter-layer interfaces are found to be less detrimental than inter-filament interfaces; and thus, it is beneficial to have wide layers (that minimize inter-filament interfaces), even if layer height has to be reduced thereby resulting in more inter-layer interfaces. When practical considerations are taken into account, a wider layer and a higher layer height are obviously better choices from printing productivity considerations as well, provided acceptable mechanical properties are attained. One more factor that has not been considered in this study is the fact that, when layer widths and heights are higher than the limits imposed in this work, NSSM test with the sample size as is commonly done might not be applicable, since the sample might not be representative.

A note on the effect of potentials used in NSSM test

The potential difference to be used in the NSSM test was arrived at based on the initial current reading obtained under a 30 V potential. Based on the initial current recorded, a 10 V potential was applied for all the NSSM tests in this study as described earlier; however most conventional concrete specimens are subjected to a 30 V potential in the NSSM test. Note that these recommendations in NT Build 492 were arrived at based on plain OPC concretes alone, and not on mortars, which were investigated in this work, or on mixtures containing cement replacement materials, even though the differences are expected to be minimal if the aggregate volume fractions are comparable. While some of the 3D printed specimens could have been subjected to a 15 V potential, in order to keep the analysis consistent, a 10 V potential was used for all the samples. For 0.35-0.40 w/b ratio concretes containing 10-15% limestone (by mass), the 28-day D_{nssm} values reported in the literature are in the range of $11\text{-}13 \times 10^{-12}$ m^2/s, while corresponding OPC concrete showed D_{nssm} values of ~14×10^{-12} m^2/s, when tested under a 30 V potential [62]–[64]. Similar values for limestone-bearing concretes have been reported in other studies as well [65]. Thus, the values obtained for the 3D printed concretes in this study, varying between $17\text{-}23 \times 10^{-12}$ m^2/s (in the D2 and D3 directions) can be considered to be reasonable, given: (i) the effects of layer and filament interfaces; and (ii) the higher limestone content, on the transport properties.

In order to examine if the lower potential used for the 3D printed specimens could have significantly influenced the D_{nssm} values (though it is obvious that the penetration depths will be affected), NSSM tests were carried out on a conventional plain concrete mixture (w/c of 0.42; cured for 56+ days) at 10, 20 and 30 V (even though a 30 V potential was recommended based on the initial current). The calculated D_{nssm} values depend on the applied potential as well as the depth of penetration, as shown in Equations 1 and 2. Figure 14 shows the plot of D_{nssm} as a function of the applied potential and penetration depth. If the penetration depths are simply related to the voltage, they scale linearly with the potential (8, 19, and 29 mm respectively for 10, 20, and 30 V potentials for the plain concrete mixture – similar to that in [66], which investigated three potentials in the 30 V to 60 V range). The calculated D_{nssm} values for these specimens were ~ 10×10^{-12} m^2/s, 13×10^{-12} m^2/s, and 14×10^{-12} m^2/s for the three potentials, with the values corresponding to the 20 V and 30 V potential being fairly close to each other. For the NSSM test, [43] recommends that the voltage needs to be adjusted to also obtain a penetration depth in excess of 10 mm, which is not satisfied here for the plain concrete mixture under a 10 V potential. When that condition is satisfied – for the 20 V and 30 V cases – the D_{nssm} values are fairly close, implying that the differences in applied potentials do not significantly alter the D_{nssm} values, a similar observation from [66] where voltages of 30 V to 60 V were used. Figure 14 also shows that D_{nssm} values increase at a significantly faster rate with penetration depth when the applied voltage is low – thus doubling of the penetration depth for a specimen subjected to 10 V implies a much higher enhancement in diffusion coefficient than for the same case when 30 V is applied. The NSSM test also assumes a linear chloride binding isotherm [67], which results in the binding of chlorides influencing the D_{nssm} values even though it has been shown that the retarding effect of binding is somewhat neutralized by the acceleration of transport in a migration test and the high upstream chloride concentrations that drive the transport [68]. Since limestone-bearing concretes bind chlorides considerably less than conventional concretes or those containing supplementary cementing materials [69], the inaccuracy in binding considerations is less likely to influence the accuracy of the NSSM results reported here. However, the coupled effect of acceleration of transport through the interfaces and retardation through binding could become important in 3D printed systems proportioned using materials capable of enhanced chloride binding (e.g., those employing carbonate-aluminate synergies [46], [70], [71], or higher volumes of fly ash), which needs to be considered in such analyses.

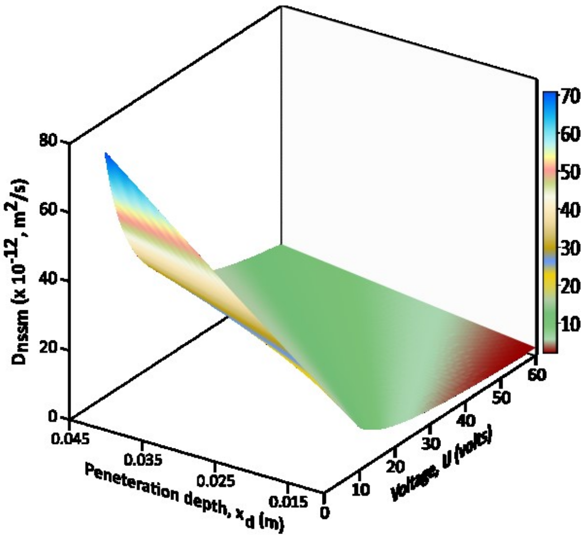

Figure 14: Dependence of D_{nssm} on the applied voltage (V) and chloride penetration depth (x_d)

4. Conclusions

This study has investigated the influence of inter-layer and inter-filament interfaces on the chloride transport resistance of 3D printed concrete specimens, using an accelerated migration test (non-steady state migration, NSSM). Two different mixtures – both containing 30% of limestone powder by mass of the binder, with one reinforced with 0.28% by volume of basalt fibers – were used for the NSSM testing. The mixtures were 3D printed with three different layer heights (6, 13, and 20 mm). The specimens were tested in the three orthogonal directions (denoted as D1, D2, and D3 in this paper) to understand the anisotropy with respect to ionic transport.

The overall capillary porosity of the 3D printed concrete specimens were found to be relatively invariant with layer heights. However, MIP results showed that porosity and critical pore sizes in the bulk region of the layers (not accounting for any of the interfaces) decreased with decreasing layer heights. The improved consolidation experienced by the bulk region in the layers, due to the higher nozzle pressures when printing thinner layers, resulted in such an observation. The mercury retention factor, R from intrusion-extrusion MIP experiments was found to be higher for samples extracted from lower layer height specimens, indicating the enhanced tortuosity in the bulk region of such layers. Electrical conductivities measured along the different directions indicated the influence of anisotropy in the electrical transport paths for 3D printed concrete specimens.

The non-steady state migration coefficients (D_{nssm}) were determined based on a 10 V potential, as dictated by the initial current. The D_{nssm} values were found to depend on the layer height and direction of testing. The D_{nssm} values for the printed samples were 10-30% higher than that of the cast samples in the D2 and D3 directions, due to the inter-layer and inter-filament defects introduced due to printing; the larger the effect when the layer heights were larger. The results in the D1 direction (along the direction of printing) were found to be unreliable because of the continuous (or nearly continuous) inter-filament channels in that direction, and thus have been neglected. Inter-filament interfaces need to be minimized to ensure desirable transport characteristics for 3D printed concrete elements, especially when they are reinforced, and thus it is beneficial to have wide layers (that minimize inter-filament interfaces). It was also shown that, when the chloride penetration depth in the sample after NSSM test (determined by spraying $AgNO_3$) was more than 10 mm, the calculated D_{nssm} values were not influenced by the voltage chosen for the test, even though D_{nssm} becomes much more sensitive to the applied voltage at lower voltages.

5. Acknowledgement

The authors sincerely acknowledge the support from U.S. National Science Foundation (CMMI: 1727445; OISE: 2020095) towards this project. The authors also acknowledge the support from Salt River Materials Group, Omya, BASF and Rock fiber in donating the materials, and the use of 3D printing and material characterization facilities within the Laboratory for the Science of Sustainable Infrastructural Materials (LS-SIM) at Arizona State University in the completion of this project.

References

[1] E. Lloret *et al.*, “Complex concrete structures: Merging existing casting techniques with digital fabrication,” *Comput.-Aided Des.*, vol. 60, pp. 40–49, Mar. 2015, doi: 10.1016/j.cad.2014.02.011.

[2] G. De Schutter, K. Lesage, V. Mechtcherine, V. N. Nerella, G. Habert, and I. Agusti-Juan, “Vision of 3D printing with concrete — Technical, economic and environmental potentials,” *Cem. Concr. Res.*, vol. 112, pp. 25–36, Oct. 2018, doi: 10.1016/j.cemconres.2018.06.001.

[3] J. Zhang, J. Wang, S. Dong, X. Yu, and B. Han, “A review of the current progress and application of 3D printed concrete,” *Compos. Part Appl. Sci. Manuf.*, vol. 125, p. 105533, Oct. 2019, doi: 10.1016/j.compositesa.2019.105533.

[4] P. Releases, “3D Concrete Printing Market to Reach $ 56.4 Million by 2021,” *3Printr.com*, Jun. 02, 2016. https://www.3printr.com/3d-concrete-printing-market-reach-56-4-million-2021-1239664/ (accessed May 12, 2022).

[5] T. Marchment, J. G. Sanjayan, B. Nematollahi, and M. Xia, “Chapter 12 - Interlayer Strength of 3D Printed Concrete: Influencing Factors and Method of Enhancing,” in *3D Concrete Printing Technology*, J. G. Sanjayan, A. Nazari, and B. Nematollahi, Eds. Butterworth-Heinemann, 2019, pp. 241–264. doi: 10.1016/B978-0-12-815481-6.00012-9.

[6] R. A. Buswell, R. C. Soar, A. G. F. Gibb, and A. Thorpe, “Freeform Construction: Mega-scale Rapid Manufacturing for construction,” *Autom. Constr.*, vol. 16, no. 2, pp. 224–231, Mar. 2007, doi: 10.1016/j.autcon.2006.05.002.

[7] C. Gosselin, R. Duballet, Ph. Roux, N. Gaudillière, J. Dirrenberger, and Ph. Morel, “Large-scale 3D printing of ultra-high performance concrete – a new processing route for architects and builders,” *Mater. Des.*, vol. 100, pp. 102–109, Jun. 2016, doi: 10.1016/j.matdes.2016.03.097.

[8] A. Kazemian, X. Yuan, E. Cochran, and B. Khoshnevis, “Cementitious materials for construction-scale 3D printing: Laboratory testing of fresh printing mixture,” *Constr. Build. Mater.*, vol. 145, pp. 639–647, Aug. 2017, doi: 10.1016/j.conbuildmat.2017.04.015.

[9] T. T. Le *et al.*, “Hardened properties of high-performance printing concrete,” *Cem. Concr. Res.*, vol. 42, no. 3, pp. 558–566, Mar. 2012, doi: 10.1016/j.cemconres.2011.12.003.

[10] G. Ji, T. Ding, J. Xiao, S. Du, J. Li, and Z. Duan, “A 3D Printed Ready-Mixed Concrete Power Distribution Substation: Materials and Construction Technology,” *Materials*, vol. 12, no. 9, p. 1540, May 2019, doi: 10.3390/ma12091540.

[11] T. T. Le, S. A. Austin, S. Lim, R. A. Buswell, A. G. F. Gibb, and T. Thorpe, “Mix design and fresh properties for high-performance printing concrete,” *Mater. Struct.*, vol. 45, no. 8, pp. 1221–1232, Aug. 2012, doi: 10.1617/s11527-012-9828-z.

[12] S. Lim, R. A. Buswell, T. T. Le, S. A. Austin, A. G. F. Gibb, and T. Thorpe, “Developments in construction-scale additive manufacturing processes,” *Autom. Constr.*, vol. 21, pp. 262–268, Jan. 2012, doi: 10.1016/j.autcon.2011.06.010.

[13] S. A. O. Nair, S. Panda, M. Santhanam, G. Sant, and N. Neithalath, “A critical examination of the influence of material characteristics and extruder geometry on 3D printing of cementitious binders,” *Cem. Concr. Compos.*, vol. 112, p. 103671, Sep. 2020, doi: 10.1016/j.cemconcomp.2020.103671.

[14] H. Alghamdi, S. A. O. Nair, and N. Neithalath, “Insights into material design, extrusion rheology, and properties of 3D-printable alkali-activated fly ash-based binders,” *Mater. Des.*, vol. 167, p. 107634, Apr. 2019, doi: 10.1016/j.matdes.2019.107634.

[15] S. A. O. Nair, H. Alghamdi, A. Arora, I. Mehdipour, G. Sant, and N. Neithalath, “Linking fresh paste microstructure, rheology and extrusion characteristics of cementitious binders for 3D printing,” *J. Am. Ceram. Soc.*, vol. 102, no. 7, pp. 3951–3964, 2019, doi: 10.1111/jace.16305.

[16] G. Ma, N. M. Salman, L. Wang, and F. Wang, “A novel additive mortar leveraging internal curing for enhancing interlayer bonding of cementitious composite for 3D printing,” *Constr. Build. Mater.*, vol. 244, p. 118305, May 2020, doi: 10.1016/j.conbuildmat.2020.118305.

[17] R. J. M. Wolfs, F. P. Bos, and T. A. M. Salet, “Hardened properties of 3D printed concrete: The influence of process parameters on interlayer adhesion,” *Cem. Concr. Res.*, vol. 119, pp. 132–140, May 2019, doi: 10.1016/j.cemconres.2019.02.017.

[18] T. Ding, J. Xiao, S. Zou, and X. Zhou, “Anisotropic behavior in bending of 3D printed concrete reinforced with fibers,” *Compos. Struct.*, vol. 254, p. 112808, Dec. 2020, doi: 10.1016/j.compstruct.2020.112808.

[19] M. Hambach and D. Volkmer, “Properties of 3D-printed fiber-reinforced Portland cement paste,” *Cem. Concr. Compos.*, vol. 79, pp. 62–70, May 2017, doi: 10.1016/j.cemconcomp.2017.02.001.

[20] A. V. Rahul, M. Santhanam, H. Meena, and Z. Ghani, “Mechanical characterization of 3D printable concrete,” *Constr. Build. Mater.*, vol. 227, p. 116710, Dec. 2019, doi: 10.1016/j.conbuildmat.2019.116710.

[21] S. A. O. Nair, A. Tripati, and N. Neithalath, “Examining layer height effects on the flexural and fracture response of plain and fiber-reinforced 3D-printed beams,” *Cem. Concr. Compos.*, vol. 124, pp. 586–601, Nov. 2021, doi: 10.1016/j.cemconcomp.2021.104254.

[22] V. N. Nerella, S. Hempel, and V. Mechtcherine, “Effects of layer-interface properties on mechanical performance of concrete elements produced by extrusion-based 3D-printing,” *Constr. Build. Mater.*, vol. 205, pp. 586–601, Apr. 2019, doi: 10.1016/j.conbuildmat.2019.01.235.

[23] S. Yu, M. Xia, J. Sanjayan, L. Yang, J. Xiao, and H. Du, “Microstructural characterization of 3D printed concrete,” *J. Build. Eng.*, vol. 44, p. 102948, Dec. 2021, doi: 10.1016/j.jobe.2021.102948.

[24] G. Ma, J. Zhang, L. Wang, Z. Li, and J. Sun, “Mechanical characterization of 3D printed anisotropic cementitious material by the electromechanical transducer,” *Smart Mater. Struct.*, vol. 27, no. 7, p. 075036, Jun. 2018, doi: 10.1088/1361-665X/aac789.

[25] A. S. Alchaar and A. K. Al-Tamimi, “Mechanical properties of 3D printed concrete in hot temperatures,” *Constr. Build. Mater.*, vol. 266, p. 120991, Jan. 2021, doi: 10.1016/j.conbuildmat.2020.120991.

[26] L. Del Giudice and M. F. Vassiliou, “Mechanical properties of 3D printed material with binder jet technology and potential applications of additive manufacturing in seismic testing of structures,” *Addit. Manuf.*, vol. 36, p. 101714, Dec. 2020, doi: 10.1016/j.addma.2020.101714.

[27] T. Ding, J. Xiao, S. Zou, and Y. Wang, “Hardened properties of layered 3D printed concrete with recycled sand,” *Cem. Concr. Compos.*, vol. 113, p. 103724, Oct. 2020, doi: 10.1016/j.cemconcomp.2020.103724.

[28] Y. Zhang *et al.*, “Relationship between water transport behaviour and interlayer voids of 3D printed concrete,” *Constr. Build. Mater.*, vol. 326, p. 126731, Apr. 2022, doi: 10.1016/j.conbuildmat.2022.126731.

[29] B. Anleu and P. C, “Quantitative Micro XRF Mapping of Chlorides: Possibilities, Limitations, and Applications, from Cement to Digital Concrete,” Doctoral Thesis, ETH Zurich, 2018. doi: 10.3929/ethz-b-000328911.

[30] J. J. Assaad, F. Hamzeh, and B. Hamad, “Qualitative assessment of interfacial bonding in 3D printing concrete exposed to frost attack,” *Case Stud. Constr. Mater.*, vol. 13, p. e00357, Dec. 2020, doi: 10.1016/j.cscm.2020.e00357.

[31] J. Van Der Putten *et al.*, “Transport properties of 3D printed cementitious materials with prolonged time gap between successive layers,” *Cem. Concr. Res.*, vol. 155, p. 106777, May 2022, doi: 10.1016/j.cemconres.2022.106777.

[32] G. M. Moelich, P. J. Kruger, and R. Combrinck, “The effect of restrained early age shrinkage on the interlayer bond and durability of 3D printed concrete,” *J. Build. Eng.*, vol. 43, p. 102857, Nov. 2021, doi: 10.1016/j.jobe.2021.102857.

[33] Y. Zhang *et al.*, “Hardened properties and durability of large-scale 3D printed cement-based materials,” *Mater. Struct.*, vol. 54, no. 1, p. 45, Feb. 2021, doi: 10.1617/s11527-021-01632-x.

[34] Y. Zhang, Y. Zhang, R. Qian, G. Liu, and H. Du, “Influence of steel fiber on the water absorption of 3D printed concrete,” *Mater. Lett.*, vol. 330, p. 133252, Jan. 2023, doi: 10.1016/j.matlet.2022.133252.

[35] Y. Zhang, Y. Zhang, L. Yang, G. Liu, and H. Du, “Evaluation of aggregates, fibers and voids distribution in 3D printed concrete,” *J. Sustain. Cem.-Based Mater.*, vol. 0, no. 0, pp. 1–14, Aug. 2022, doi: 10.1080/21650373.2022.2113168.

[36] B. Panda, S. Chandra Paul, and M. Jen Tan, “Anisotropic mechanical performance of 3D printed fiber reinforced sustainable construction material,” *Mater. Lett.*, vol. 209, pp. 146–149, Dec. 2017, doi: 10.1016/j.matlet.2017.07.123.

[37] Y. Chen, Y. Zhang, B. Pang, Z. Liu, and G. Liu, “Extrusion-based 3D printing concrete with coarse aggregate: Printability and direction-dependent mechanical performance,” *Constr. Build. Mater.*, vol. 296, p. 123624, Aug. 2021, doi: 10.1016/j.conbuildmat.2021.123624.

[38] B. Zahabizadeh, J. Pereira, C. Gonçalves, E. N. B. Pereira, and V. M. C. F. Cunha, “Influence of the printing direction and age on the mechanical properties of 3D printed concrete,” *Mater. Struct.*, vol. 54, no. 2, p. 73, Mar. 2021, doi: 10.1617/s11527-021-01660-7.

[39] M. van den Heever, A. du Plessis, J. Kruger, and G. van Zijl, “Evaluating the effects of porosity on the mechanical properties of extrusion-based 3D printed concrete,” *Cem. Concr. Res.*, vol. 153, p. 106695, Mar. 2022, doi: 10.1016/j.cemconres.2021.106695.

[40] ASTM International, “Standard Specification for Limestone Dimension Stone,” ASTM International, West Conshohocken, PA, 2022. Accessed: Oct. 25, 2022. [Online]. Available: https://www.astm.org/c0568_c0568m-22.html

[41] ASTM International, “Standard Specification for Standard Sand,” ASTM International, West Conshohocken, PA, 2021. Accessed: Oct. 25, 2022. [Online]. Available: https://www.astm.org/c0778-21.html

[42] S. Nair, S. Panda, A. Tripathi, and N. Neithalath, “Relating print velocity and extrusion characteristics of 3D-printable cementitious binders: Implications towards testing methods,” *Addit. Manuf.*, vol. 46, p. 102127, Oct. 2021, doi: 10.1016/j.addma.2021.102127.

[43] “NT Build 492, Concrete, Mortar and Cement-Based Repair Materials: Chloride Migration Coefficient from Non-Steady-State Migration Experiments,” Nord Test Method, 1999.

[44] RILEM, “CPC 11.3, Absorption of water by immersion under vacuum,” Mater. Struct. 17, 1984.

[45] D. Ravikumar and N. Neithalath, “An electrical impedance investigation into the chloride ion transport resistance of alkali silicate powder activated slag concretes,” *Cem. Concr. Compos.*, vol. 44, pp. 58–68, Nov. 2013, doi: 10.1016/j.cemconcomp.2013.06.002.

[46] M. Aguayo, P. Yang, K. Vance, G. Sant, and N. Neithalath, “Electrically driven chloride ion transport in blended binder concretes: Insights from experiments and numerical simulations,” *Cem. Concr. Res.*, vol. 66, pp. 1–10, Dec. 2014, doi: 10.1016/j.cemconres.2014.07.022.

[47] ASTM International, “ASTM C1876-19 Standard Test Method for Bulk Electrical Resistivity or Bulk Conductivity of Concrete,” ASTM International, West Conshohocken, PA, 2019. [Online]. Available: https://doi.org/10.1520/C1876-19

[48] D. Winslow, “Some Experimental Possibilities With Mercury Intrusion Porosimetry,” *MRS Online Proc. Libr.*, vol. 137, no. 1, pp. 93–103, Dec. 1988, doi: 10.1557/PROC-137-93.

[49] R. Feldman, “Pore Structure Damage in Blended Cements Caused by Mercury Intrusion,” *J. Am. Ceram. Soc.*, vol. 67, Oct. 2006, doi: 10.1111/j.1151-2916.1984.tb19142.x.

[50] Y. Chen, F. Al-Neshawy, and J. Punkki, “Investigation on the effect of entrained air on pore structure in hardened concrete using MIP,” *Constr. Build. Mater.*, vol. 292, p. 123441, Jul. 2021, doi: 10.1016/j.conbuildmat.2021.123441.

[51] Q. Zeng, K. Li, T. Fen-Chong, and P. Dangla, “Analysis of pore structure, contact angle and pore entrapment of blended cement pastes from mercury porosimetry data,” *Cem. Concr. Compos.*, vol. 34, no. 9, pp. 1053–1060, Oct. 2012, doi: 10.1016/j.cemconcomp.2012.06.005.

[52] F. Moro and H. Böhni, “Ink-Bottle Effect in Mercury Intrusion Porosimetry of Cement-Based Materials,” *J. Colloid Interface Sci.*, vol. 246, no. 1, pp. 135–149, Feb. 2002, doi: 10.1006/jcis.2001.7962.

[53] K. Vance, “Early age characterization and microstructural features of sustainable binder systems for concrete,” Arizona State University, 2014. Accessed: Aug. 04, 2022. [Online]. Available: https://keep.lib.asu.edu/items/152842

[54] J. Zhang, F. Bian, Y. Zhang, Z. Fang, C. Fu, and J. Guo, “Effect of pore structures on gas permeability and chloride diffusivity of concrete,” *Constr. Build. Mater.*, vol. 163, pp. 402–413, Feb. 2018, doi: 10.1016/j.conbuildmat.2017.12.111.

[55] Y. Guo, X. Hu, and J. Lv, “Experimental study on the resistance of basalt fibre-reinforced concrete to chloride penetration,” *Constr. Build. Mater.*, vol. 223, pp. 142–155, Oct. 2019, doi: 10.1016/j.conbuildmat.2019.06.211.

[56] F. Koksal, E. T. Kocabeyoglu, O. Gencel, and A. Benli, “The effects of high temperature and cooling regimes on the mechanical and durability properties of basalt fiber reinforced mortars with silica fume,” *Cem. Concr. Compos.*, vol. 121, p. 104107, Aug. 2021, doi: 10.1016/j.cemconcomp.2021.104107.

[57] O. Yavuz Bayraktar, G. Kaplan, O. Gencel, A. Benli, and M. Sutcu, “Physico-mechanical, durability and thermal properties of basalt fiber reinforced foamed concrete containing waste marble powder and slag,” *Constr. Build. Mater.*, vol. 288, p. 123128, Jun. 2021, doi: 10.1016/j.conbuildmat.2021.123128.

[58] Y. Zeng, X. Zhou, A. Tang, and P. Sun, “Mechanical Properties of Chopped Basalt Fiber-Reinforced Lightweight Aggregate Concrete and Chopped Polyacrylonitrile Fiber Reinforced Lightweight Aggregate Concrete,” *Materials*, vol. 13, no. 7, Art. no. 7, Jan. 2020, doi: 10.3390/ma13071715.

[59] D. Niu, L. Su, Y. Luo, D. Huang, and D. Luo, “Experimental study on mechanical properties and durability of basalt fiber reinforced coral aggregate concrete,” *Constr. Build. Mater.*, vol. 237, p. 117628, Mar. 2020, doi: 10.1016/j.conbuildmat.2019.117628.

[60] P. R. da Silva and J. de Brito, “Durability performance of self-compacting concrete (SCC) with binary and ternary mixes of fly ash and limestone filler,” *Mater. Struct.*, vol. 49, no. 7, pp. 2749–2766, Jul. 2016, doi: 10.1617/s11527-015-0683-6.

[61] N. Neithalath and H. T. Cam, “Strength and Transport Properties of Concretes Modified with Coarse Limestone Powder to Compensate for Dilution Effects,” *Transp. Res. Rec.*, vol. 2290, no. 1, pp. 130–138, Jan. 2012, doi: 10.3141/2290-17.

[62] H. T. Cam and N. Neithalath, “Moisture and ionic transport in concretes containing coarse limestone powder,” *Cem. Concr. Compos.*, vol. 32, no. 7, pp. 486–496, Aug. 2010, doi: 10.1016/j.cemconcomp.2010.04.002.

[63] Y. Dhandapani and M. Santhanam, “Investigation on the microstructure-related characteristics to elucidate performance of composite cement with limestone-calcined clay combination,” *Cem. Concr. Res.*, vol. 129, p. 105959, Mar. 2020, doi: 10.1016/j.cemconres.2019.105959.

[64] Y. Dhandapani, T. Sakthivel, M. Santhanam, R. Gettu, and R. G. Pillai, “Mechanical properties and durability performance of concretes with Limestone Calcined Clay Cement (LC3),” *Cem. Concr. Res.*, vol. 107, pp. 136–151, May 2018, doi: 10.1016/j.cemconres.2018.02.005.

[65] A. H. Yadak Yaraghi, A. M. Ramezanianpour, A. A. Ramezanianpour, F. Bahman-Zadeh, and A. Zolfagharnasab, “Evaluation of test procedures for durability and permeability assessment of concretes containing calcined clay,” *J. Build. Eng.*, p. 105016, Jul. 2022, doi: 10.1016/j.jobe.2022.105016.

[66] P. Spiesz and H. J. H. Brouwers, “Influence of the applied voltage on the Rapid Chloride Migration (RCM) test,” *Cem. Concr. Res.*, vol. 42, no. 8, pp. 1072–1082, Aug. 2012, doi: 10.1016/j.cemconres.2012.04.007.

[67] M. Castellote, C. Andrade, and C. Alonso, “Chloride-binding isotherms in concrete submitted to non-steady-state migration experiments,” *Cem. Concr. Res.*, vol. 29, no. 11, pp. 1799–1806, Nov. 1999, doi: 10.1016/S0008-8846(99)00173-8.

[68] P. Yang, G. Sant, and N. Neithalath, “A refined, self-consistent Poisson-Nernst-Planck (PNP) model for electrically induced transport of multiple ionic species through concrete,” *Cem. Concr. Compos.*, vol. 82, pp. 80–94, Sep. 2017, doi: 10.1016/j.cemconcomp.2017.05.015.

[69] C. Li and L. Jiang, “The role of chloride binding mechanism in the interpretation of chloride profiles in concrete containing limestone powder,” *J. Sustain. Cem.-Based Mater.*, vol. 0, no. 0, pp. 1–12, Jan. 2022, doi: 10.1080/21650373.2021.2010243.

[70] K. Vance, M. Aguayo, T. Oey, G. Sant, and N. Neithalath, “Hydration and strength development in ternary portland cement blends containing limestone and fly ash or metakaolin,” *Cem. Concr. Compos.*, vol. 39, pp. 93–103, May 2013, doi: 10.1016/j.cemconcomp.2013.03.028.

[71] P. Yang, Y. Dhandapani, M. Santhanam, and N. Neithalath, “Simulation of chloride diffusion in fly ash and limestone-calcined clay cement (LC3) concretes and the influence of damage on service-life,” *Cem. Concr. Res.*, vol. 130, p. 106010, Apr. 2020, doi: 10.1016/j.cemconres.2020.106010.